IEEE Access
Multidisciplinary ⋮ Rapid Review ⋮ Open Access Journal

Received 22 November 2022, accepted 26 December 2022, date of publication 3 January 2023, date of current version 9 January 2023.

Digital Object Identifier 10.1109/ACCESS.2022.3233867

RESEARCH ARTICLE

Compact Substrate Integrated Waveguide Wideband Bandpass Filter With Post-Manufacturing Tuning Capabilities

EL MEHDI MESSAOUDI[1], (Student Member, IEEE), JORGE DANIEL MARTÍNEZ PEREZ[2], (Member, IEEE), AND VICENTE E. BORIA[1], (Fellow, IEEE)

[1]Institute of Telecommunications and Multimedia Applications, Universitat Politècnica de València, 46022 Valencia, Spain
[2]I3M, Universitat Politècnica de València, 46022 Valencia, Spain

Corresponding authors: El Mehdi Messaoudi (elmes@upvnet.upv.es), Jorge Daniel Martínez Perez (jdmartinez@eln.upv.es), and Vicente E. Boria (vboria@dcom.upv.es)

This work was supported in part by the European's Union Horizon 2020 Research and Innovation Programme under the Marie Sklodowska-Curie Innovative Triangle Networks (ITN) through TESLA under Grant 811232, in part by the European Space Agency (ESA) under Contract 4000124983, in part by the Ministerio de Ciencia e Innovación (MICIN) through Spanish Government under the Research and Development Project PID2019-103982R-C41 and Project MICIN/AEI/10.13039/501100011033, and in part by the funding for open access charge: Universitat Politècnica de València.

ABSTRACT In this paper, a miniaturized wideband bandpass filter in coaxial substrate integrated waveguide (SIW) technology is presented. To improve the response selectivity and coupling control, a multi-layer structure has been implemented, introducing both strong magnetic and electric couplings. To reduce the physical size of the device, surfaced-mounted device (SMD) capacitors have been integrated on the top layer. These allow both resonant frequency and capacitive coupling level control. Thus, a 4-th order Chebyshev filter with an absolute bandwidth (BW) of 2.9 GHz centered at 5.35 GHz has been designed, fabricated and measured. An extremely small filter size of 7×7 mm^2 has been obtained. A study of manufacturing tolerances are also presented in this paper, together with a post-manufacturing response correction allowed by the SMD elements. As it is shown in the paper, the filter's out-of-band rejection can be easily enhanced by introducing additional transmission zeros (TZs).

INDEX TERMS Substrate integrated waveguide (SIW), miniaturization, multi-layer, wideband, transmission zero, mixed coupling.

I. INTRODUCTION

Miniaturization of microwave passive components is a critical challenge in designing and developing communication equipment and subsystems for several emerging applications. Due to their size, antennas, filters, and diplexers are the most challenging components integrating the modern radio frequency (RF) units. Therefore, low loss, small size, and batch manufacturing are essential features to be addressed.

Substrate integrated waveguide (SIW) technology is already a consolidated alternative, providing a higher Q-factor than planar implementations and a smaller size than classic metallic waveguides [1]. However, additional miniaturization efforts are required, particularly at microwave frequencies. Moreover, this must be achieved while keeping the advantages of conventional printed circuit boards (PCBs), and of related manufacturing techniques such as the low-temperature co-fired ceramics (LTCC) manufacturing technology.

Several approaches have been proposed in the literature for producing compact SIW filters. Half-mode and folded structures can reduce their size by a factor of two [2], [3], [4], [5]. While folded cavities keep the field distribution unchanged, only modifying the field path, half-mode implementations alter the electromagnetic (EM) field distribution as the structure is split in half at its plane of symmetry. Subsequent similar implementations, such as quarter-mode [6], [7] and eighth-mode [8] have also been proposed.

The associate editor coordinating the review of this manuscript and approving it for publication was Mohamed Kheir.

Another method has been presented in [9], where individual resonant cavities are loaded with dielectric rods. Thus, a size reduction of 70% compared to the classical SIW implementation can be obtained, while maintaining good electromagnetic performance. A SIW filter loaded with complementary split-ring resonators (CSRRs) has also been presented in [10]. Thanks to CSRRs, it is possible to operate below the cut-off frequency, while different passband characteristics can be obtained thanks to their orientation. A further method for miniaturizing the device is obtained by vertically stacking SIW cavities [11]. In this case, the area size is reduced, increasing the total thickness of the filter. A SIW cavity loaded with stubs has been proposed in [12]. Again, the device can operate below the cut-off frequency. The stubs are magnetically coupled to the cavity. A reduction of about half of the unloaded SIW cavity size can be achieved. Lastly, dual-mode filters reduce the number of cavities by half, and allow the implementation of transmission zeros (TZs) [13]. The resonant cavities can also be capacitively loaded to decrease the resonance frequency (or reduce the corresponding size). Thus, filters with capacitive posts are found in [14]. Coaxial SIW structures have been proposed to reduce the resonator size, implementing the combline resonator concept of classic waveguide technology into the novel SIW one [15]. However, although these and more compact SIW implementations have been proposed, they are still relatively large compared to microstrip technology, and further miniaturization is required.

This paper presents a miniaturized wideband bandpass filter based on a quasi-lumped implementation of a coaxial SIW resonator topology initially proposed in [16] and [17]. Lumped elements are employed to lower the resonant frequency, and boost the input/output and inter-resonator couplings of the filter. Moreover, TZs can be easily obtained by combining lumped and distributed couplings. The hybrid nature of the proposed structure also allows static reconfiguration or post-manufacturing tuning of the filter response. Thus, a detailed study of the filter topology is performed, also focusing on the related post-manufacturing tuning capabilities. Therefore, back-simulation has been done to correct the response shift due to manufacturing tolerance effects. A second filtering structure with an additional TZ to improve the upper-band rejection has been designed, manufactured, and tested. Again, a further post-fabrication tuning process has been carried out to recover the filter target response.

In Section II, the proposed structure of the individual resonator is presented and analyzed, showing the different mechanisms that can be employed for the resonant frequency tuning. A detailed study of the ohmic losses in the structure is also performed, by analyzing the unloaded Q-factor as a function of the main layout parameters. Section III presents the procedure for designing and optimizing UWB filters based on the proposed resonant structure. A design example is described in detail in Section IV, showing how measured response deviations can be corrected by employing the post-manufacturing tuning capabilities of the filtering device. Next, in Section V, a new prototype with an enhanced out-of-band response (thanks to the generation of an extra TZ) is shown. Similar manufacturing issues, attributed to the use of the same fabrication batch, are also observed in this second filter prototype. Lastly, the main conclusions of this work are drawn in Section VI.

II. RESONATOR STRUCTURE

The basic structure of the resonator is shown in Fig. 1 [17]. A rectangular patch is connected to the bottom ground plane through a plated hole placed at the center of the cavity. The patch is isolated from the top plane by an air gap that behaves as a quasi-lumped capacitor C_r. The inner plated hole, with length h embedded in the dielectric substrate, behaves as a quasi-lumped inductor L_r. The via hole diameter d_h and the distance to the cavity walls affect the value of L_r. The capacitive or inductive part of the resonator can be easily modified to control the cavity resonant frequency through the corresponding layout parameters.

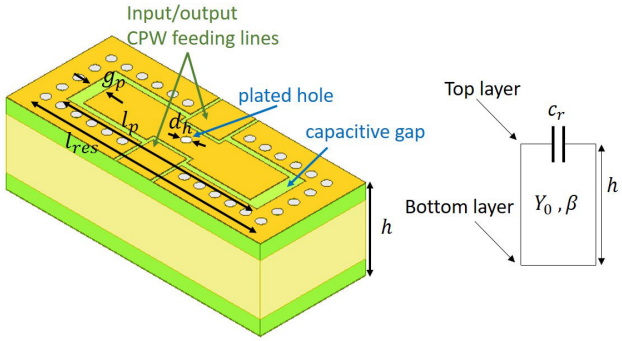

FIGURE 1. Resonator structure (left) of a single resonator and its equivalent circuit (right).

As shown in Fig. 1, the layout of the resonator is designed to minimize the area. Thus, the patch size is set to the maximum value, minimizing the distance from the cavity via holes to the capacitive gap. A more compact structure compared to the classical coaxial SIW technology [15] can be obtained. As shown in Fig. 2, lumped-element SMD capacitors can be easily mounted on the top layer to reach further miniaturization. After manufacturing, these elements also make possible the resonant frequency tunability to correct the response variations due to fabrication tolerances. Thus, replacing the SMD

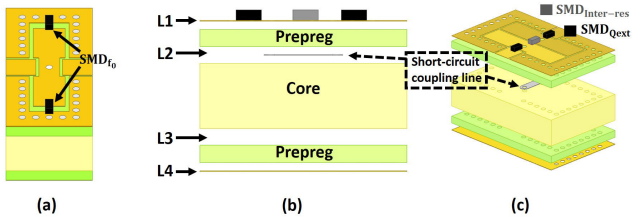

FIGURE 2. Resonator structure with resonance frequency control SMD elements (a), and second order structure stack-up (b)-(c).

capacitors with different values can fix the resonant response without further device fabrication. During the design phase, the resonant frequency can be finely tuned by adjusting the gap in the top layer or the rectangular patch perimeter.

On the other hand, the inductive part is given by the central plated via, so its length or diameter cannot be modified. It must be fixed at the beginning of the design process by choosing the proper substrate thickness and the drilling tool diameter. The easily accessible and adjustable resonator capacitance is one of the main advantages of the proposed resonant structure.

A multi-layer implementation of the structure has also been considered (see Fig. 2) to introduce strong magnetic couplings between adjacent resonators using inductive probes. As discussed in Section III, this will enable the design of broadband filters and the introduction of transmission zeros (TZs) that improve filter selectivity. Thus, the 4−layer stackup comprises two thin pre-preg (PP) layers and a central dielectric core. Apart from the top and bottom metal layers, internal conductor layers can be introduced between the PP layers and the dielectric core for implementing a substrate-integrated magnetic coupling.

The resonant frequency of the structure can be obtained as $\omega_0 = 1/\sqrt{L_r C_r}$, where C_r is the total capacitance given by the SMD capacitor and the capacitive gap. The inner via hole can be modeled as a lumped inductor considering a short section of a TEM-mode transmission line separated at a distance $l_{res}/2$ from the grounded cavity walls [18]:

$$L_r = \frac{\eta_0 h}{2\pi c_0} \ln \frac{4 l_{res}}{\pi d_h} \tag{1}$$

with c_0 the speed of light in vacuum and η_0 the wave impedance in free space. Electric and magnetic fields of the resonator (designed to have a resonant frequency of 5.35 GHz) are shown in Fig. 3. As expected, the electric field is mainly concentrated around the capacitive gap, with a current that flows in the central plated inductive via.

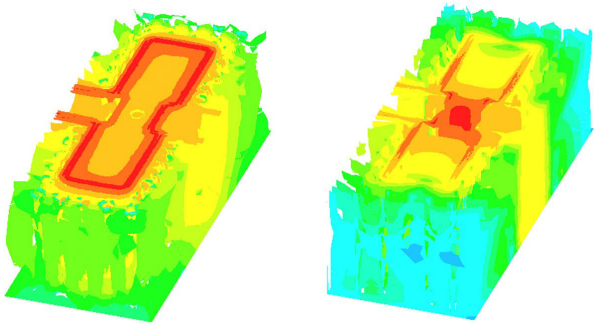

FIGURE 3. Electric (left) and magnetic (right) fields simulated with 3D EM ANSYS HFSS simulator.

A. RESONANT FREQUENCY

The three main parameters that enable control of the resonant frequency are the inner via diameter, the capacitive gap, and the cavity/patch size. A study of a single resonator has been carried out using 3D EM full-wave simulations. Increasing the cavity (and patch) size decreases the resonance frequency (Fig. 4(a)). The inductive value, whose most significant contribution is given by the central via, can be modified by changing its length (i.e., the thickness of the dielectric substrate) or its diameter. Thus, larger diameters lead to lower equivalent inductance and a higher resonant frequency. A range of radius variation from 0.15 mm to 2 mm results in an enormous tuning of the resonant frequency from 3.66 GHz to 7.79 GHz.

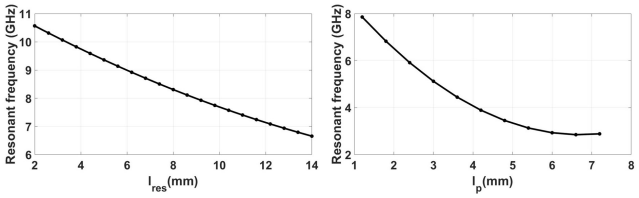

(a) Variation of f_0 in relation with the square cavity side l_{res} (left) and the square gap side l_p (right).

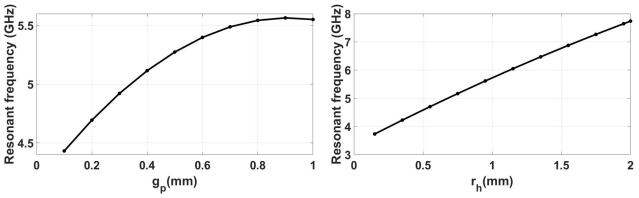

(b) Variation of f_0 in relation with the square capacitive gap width (left) and the inner plated hole radius (right).

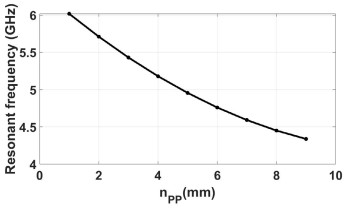

(c) Variation of f_0 in relation with the PP dielectric layers number n_{PP} .

FIGURE 4. Resonant frequency variation depending on design parameters. Second-order polynomial interpolation was adopted to plot the graphs.

Moreover, as shown in Fig. 4(c), the resonant frequency can also be controlled by increasing the thickness of the substrate. The number of PP layers n_{PP} can be modified to do this. Up to 9 layers have been considered for the inner dielectrics, giving a total thickness (i.e., including the central dielectric core) ranging from 1.726 mm to 3.342 mm. As a result, the resonance frequency shifts from 6.03 GHz to 4.32 GHz.

Similarly, a larger patch perimeter l_p increases the total capacitance, while the effect of increasing the isolating gap g_p is the opposite. As previously mentioned, SMD capacitors can be assembled on the top layer to further load the cavity, thus decreasing resonator physical size.

In Fig. 5, the resonant frequency variation is shown as a function of the capacitive gap g_p and the value of the assembled capacitors. As can be seen, capacitor values ranging from

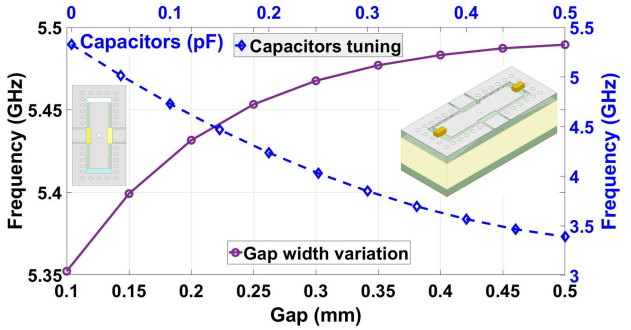

FIGURE 5. Resonant frequency as a function of the gap width (solid purple) and tuning capacitors (dashed blue). A gap width of 0.1 mm has been considered for the analysis of the variation with the SMD capacitor values.

50 to 500 fF allow a reduction of the resonant frequency from around 5.5 down to 3.5 GHz, while keeping all other resonator dimensions constant. Lastly, the capacitance gaps can also be used for finely tuning the resonant frequency.

B. UNLOADED QUALITY FACTOR

The main contributors to the ohmic losses in a conventional SIW structure are the conductor and dielectric lossy materials, as well as radiation leakage. Once radiation losses are properly minimized by selecting a convenient diameter and pitch for the plated wall vias [19], the unloaded quality factor is essentially related to the metal and dielectric material properties.

Thus, SIW technology losses are generally higher than for an empty metallic waveguide, but usually lower than for microstrip counterparts. For instance, SIW filters can achieve unloaded quality factors up to 800 [16] when using low-loss dielectric materials and excellent conductors.

The unloaded quality factor of the resonator can be expressed as:

$$\frac{1}{Q_{res}} = \frac{1}{Q_{cond}} + \frac{1}{Q_{diel}} + \frac{1}{Q_{rad}} \tag{2}$$

where Q_{cond} represents conductor, Q_{diel} dielectric, and Q_{rad} radiation losses, respectively. The quality factor of the structure, also taking into account the assembled SMD elements, is finally given by:

$$\frac{1}{Q_{tot}} = \frac{1}{Q_{res}} + \frac{1}{Q_{smd}} \tag{3}$$

Thus, a single square resonator quality factor study using 3D EM full-wave simulations has been carried out. The unloaded Q-factor has been obtained from the transmission response of a loosely coupled resonator.

In Fig. 6, the extracted unloaded Q-factor is studied as a function of the main layout parameters. As can be seen, an increase in the cavity size (i.e., l_{res}) from 2 to 14 mm results in Q-factor variation from 218 up to 266. The corresponding shift in the resonance frequency goes from 10.69 to 6.64 GHz (see Fig. 4). On the contrary, as the patch size given by

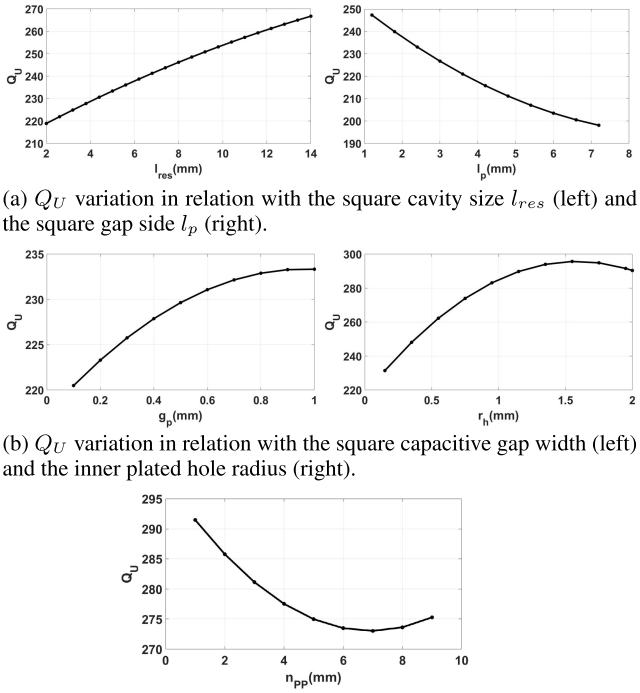

(a) Q_U variation in relation with the square cavity size l_{res} (left) and the square gap side l_p (right).

(b) Q_U variation in relation with the square capacitive gap width (left) and the inner plated hole radius (right).

(c) Q_U variation in relation with the PP dielectric layers number n_{PP} .

FIGURE 6. Unloaded quality factor (Q_U) depending on design parameters. Second-order polynomial interpolation was adopted to trace the graphs.

l_p increases, the Q-factor is reduced. At the same time, the Q-factor is not critically affected by the isolating gap. Lastly, as can be seen in Fig. 6(b), increasing the inner conductor diameter produces a higher quality factor.

Then, to achieve the highest possible Q-factor, it is advisable to reduce the patch size, resulting in larger cavity sizes for a given resonant frequency. Therefore, a trade-off solution must be considered taking into account both Q-factor and miniaturization requirements. As can be seen in Fig. 7, for the same resonant frequency, a more compact rectangular geometry can be obtained by adjusting the cavity size to the patch size at the minimum value, without producing a significant

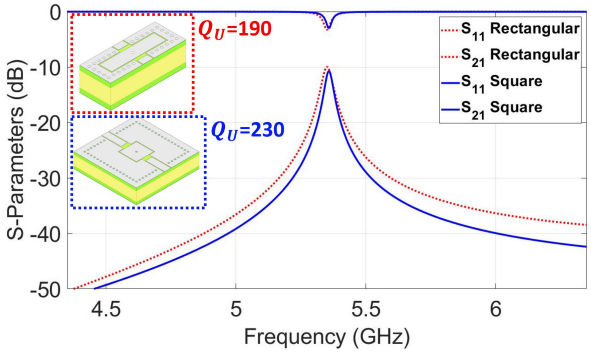

FIGURE 7. Perfectly symmetric square resonator (blue) and rectangular compact resonator (red) 3D EM Ansys HFSS simulations.

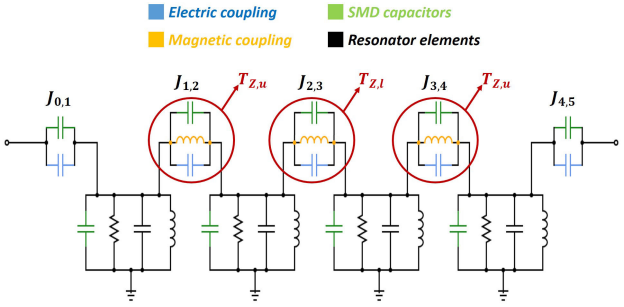

FIGURE 8. Circuit schematic of a 4-th order filter.

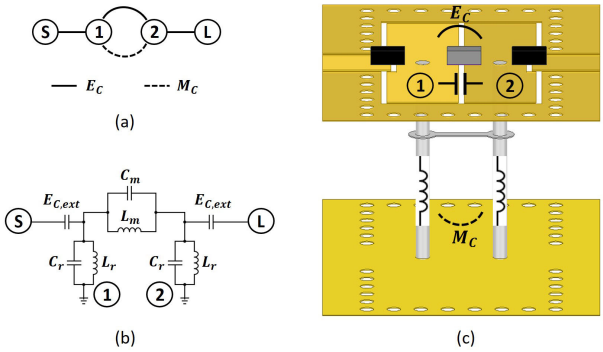

FIGURE 9. Coupling topology (a), equivalent lumped model circuit (b), and two coupled resonators 3D structure without the dielectric blocks.

decrease of the unloaded Q-factor (i.e., from 230 to 190). This work has exploited this advantage to obtain a very high degree of miniaturization without affecting the filter performance.

III. WIDEBAND BANDPASS FILTER DESIGN

A wideband bandpass filter can be designed by the cascaded connection of several coupled resonators. Thus, the input/output and inter-resonator couplings have been studied to enable an initial dimensioning of the filter for a given targeted response. Similar to the resonator capacitance, SMD capacitors have been conveniently assembled on the top layer to increase the coupling intensity, while allowing further control for the practical implementation of both input/output and inter-resonator couplings. An equivalent circuit of 4 cascaded coupled resonators is shown in Fig. 8. By implementing mixed couplings between some of the resonators, it is possible to add transmission zeros (TZs) that improve the selectivity of the filter response.

A. MIXED COUPLING ANALYSIS

From a general point of view, the overall coupling is always given by the superposition of the magnetic and electrical contribution [20]:

$$k \approx E_C + M_C \tag{4}$$

Thus, it is possible to assess the total contribution of the couplings using 3D EM simulation software, studying the couplings as a result of the E_C and M_C superposition. The required inter-resonator coupling coefficients values k_{ij} can be obtained from the inverter-coupled equivalent circuit theory as proposed in [21]

$$k_{ij} = \frac{J_{ij}}{\omega_0 Cr} \tag{5}$$

where J_{ij} is the inverter coefficient between resonators i and j, while C_r is the capacitance of the shunt resonator. However, this design theory does not consider the transmission zeros that can appear in the filter response when the electric and magnetic couplings are equal at a particular frequency, thus canceling each other. In [22] and [23], the mixed coupling circuit design theory, including the TZs analysis, has been developed. Fig. 9 shows the coupling topology (a), the equivalent lumped model circuit (b), and the 3D structure of the two coupled resonators without the dielectric blocks (c). According to the EM mixed theory proposed in [23], the mixed coupling coefficient of the circuit model in Fig. 9(b) is:

$$k = \frac{M_C - E_C}{1 - M_C E_C} \tag{6}$$

where M_C and E_C are the magnetic and electric coupling contribution respectively, and are equivalent to:

$$E_C = \frac{C_m}{C_r + C_m} \qquad M_C = \frac{L_r}{L_r + L_m} \tag{7}$$

From the equivalent circuit model in Fig. 9(b) it is possible to derive the angular frequency at which the transmission zero appears:

$$\omega_z = \frac{1}{\sqrt{L_m C_m}} \tag{8}$$

The magnetic and electric mixed-coupling contribution in the proposed topology has been studied using two coupled resonators. The stack-up of the second-order filtering structure is shown in Fig. 2(b)-(c). The device is designed in multi-layer technology, with two top and bottom 17 μm copper layers that enclose two 0.404 mm-thick RO4350B ($\epsilon_r = 3.55$, $\tan\delta = 0.0037$) pre-preg (PP) layers, and a dielectric core of 1.524 mm-thick RO4003C ($\epsilon_r = 3.55$, $\tan\delta = 0.0027$). The capacitive coupling contribution can be modified by widening the capacitive gap between the two resonators. Additionally, SMD capacitors mounted on the capacitive gap between adjacent resonators allow the coupling value control (see Fig. 10(b)). The magnetic contribution can be controlled by moving the inner plated holes closer together (or further apart). Layers L_2 and L_3 are used to implement the 17 μm copper striplines that short-circuit the two inner conductors of the adjacent resonators, obtaining a strong magnetic coupling [24]. The point where the short-circuit is realized (i.e., the distance from the top layer) significantly influences the inductive coupling value, as does the width of the stripline. The wider the trace, the greater the coupling effect (see Fig. 10(a)). As shown in Fig. 10(b), when the short circuit occurs in the inner lower layer (dashed line) or is not implemented (as in Fig. 10(c)), the electric coupling contribution dominates over the magnetic one, as it

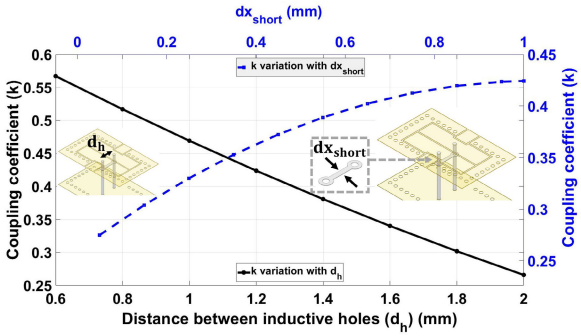

(a) Dominant magnetic coupling contribution (i.e. short stripline in L_2). Coupling coefficient variation with respect to the stripline probe width dx_{short} ($d_h = 1.4$ mm), and the distance between inner holes d_h ($dx_{short} = 0.5$ mm).

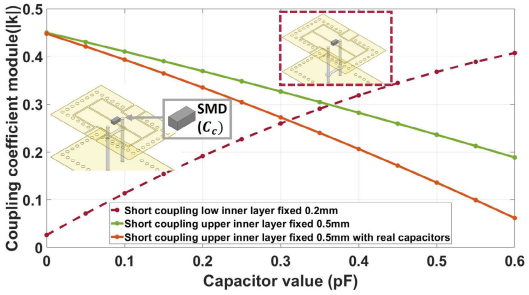

(b) Variation of the coupling coefficient with ideal and real SMD capacitor mounted on the top layer, d_h fixed. The stripline is implemented in the lower inner layer (L_3) in the first case (dashed line), while it is implemented in layer L_2 in the other two cases (solid lines).

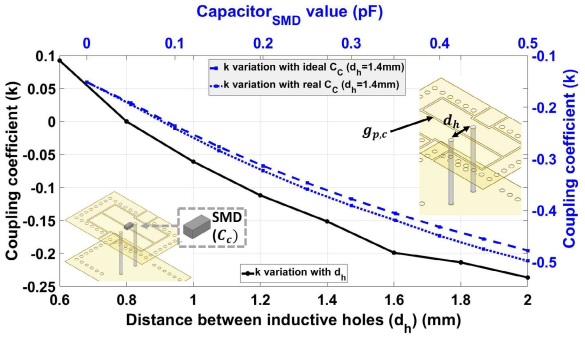

(c) Dominant electric coupling contribution (i.e. without the stripline probe). Variation of the coupling coefficient with respect to ideal and real SMD capacitor values mounted on the top layer (dashed blue lines), and with respect to d_h (with $C_c = 0$ pF and $g_{p,c} = 0.1$ mm; solid black line.)

FIGURE 10. Inter-resonators coupling.

is clear from the slope of the curve. When the short circuit is implemented in the upper inner layer L_2 (as shown in Fig. 10(a) and solid lines in Fig. 10(b)), the magnetic coupling contribution dominates.

If the electrical coupling dominates, the transmission zero appears in the lower stopband. As the magnetic contribution increases, bringing the two plated holes closer together, the total equivalent coupling decreases, and the zero shifts to

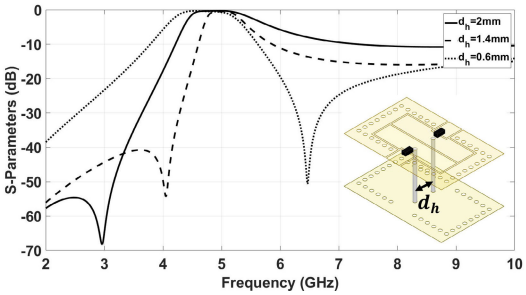

FIGURE 11. S_{21} with different distances between the two inner plated inductive holes.

higher frequencies. With 3D EM simulations of the structure, different d_h values have been studied. As shown in Fig. 11, when the magnetic contribution exceeds the electrical one, as for $d_h = 0.6$ mm, M_c becomes greater than E_c, and the transmission zero shifts to the upper stopband.

As mentioned above, a strong magnetic coupling has been implemented by adding a copper layer to short-circuit the two inductive vias using the stripline probe. As shown in Fig. 12, the magnetic contribution becomes dominant in this configuration, and the transmission zero (TZ) appear in the upper stopband. Three cases have been simulated to better understand the coupling behavior in this configuration. To evaluate f_{ev} and f_{od}, the structure has been uncoupled at the input/output ($C_{ext} = 0$ pF, Fig.12(a)). At the same time, to obtain the filtering response in Fig. 12(b), the two input/output SMD capacitances have been adjusted to achieve sufficient coupling. Increasing the inductive value by increasing dx_{short} from 0.05 mm to 0.95 mm increases the total equivalent coupling, so does the bandwidth and the TZ shifts to higher frequencies. Increasing the electrical contribution by increasing C_C, on the other hand, decreases the equivalent mixed coupling, as does the bandwidth. The transmission zero moves then to lower frequencies.

It is possible to control the position of the transmission zero without affecting the filter bandwidth. In fact, if the electric and magnetic contributions increase or decrease by the same value, the resultant equivalent mixed coupling value does not change, and consequently neither does the bandwidth. However, the individual contributions increase or decrease, changing the position of the transmission zero (Eq. 8). Once the filter response has been designed in the passband, the position of the zeros can be changed independently. As shown in Fig. 13, different simulations with $dx_{short} = [0.05, 0.15, 0.45, 0.95]$ mm have been carried out, proving the aforementioned feature. The transmission zeros appears at frequencies $f_z = [10, 9.38, 8.70, 8.14]$ GHz, respectively. The SMD inter-resonator coupling values are $C_c = [0, 0.1, 0.25, 0.45]$ pF, with input SMD capacitors fixed at $C_{ext} = 0.45$ pF to enable the necessary input coupling.

In summary, it can be stated that:

1) When the electric coupling dominates ($E_c > M_c$), then $k < 0$ and the TZ appears at the lower stopband.

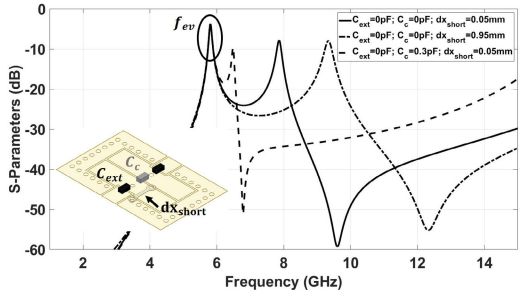

(a) Uncoupled resonators S_{21} parameters with different stripline probe width, for k evaluation.

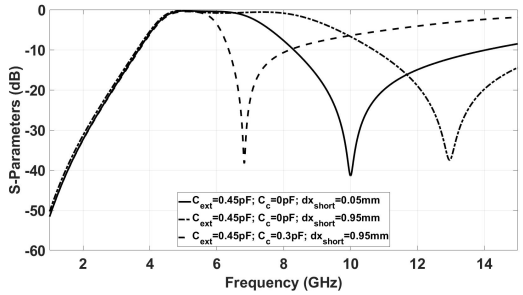

(b) S_{21} parameters with different stripline probe width.

FIGURE 12. Coupled and uncoupled resonators S_{21} parameters with different stripline probe width.

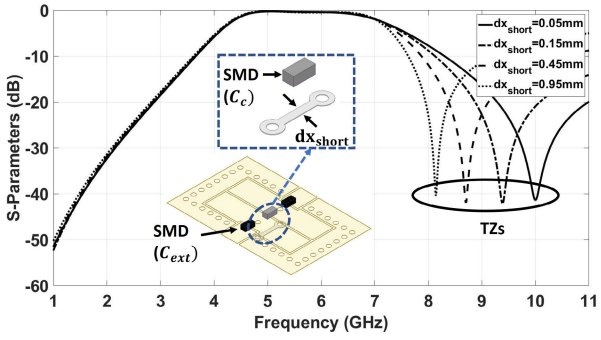

FIGURE 13. S_{21} with different transmission zero (TZ) positions, maintaining constant BW.

Increasing the magnetic contribution and keeping the electric one fixed, the equivalent mixed coupling $|k|$ decreases in module, as do the BW, and the TZ shift to higher frequency. Increasing both equally in magnitude, the TZ moves to higher frequencies without affecting the passband. On the other hand, by increasing the electric contribution and maintaining the magnetic one fixed, $|k|$ increases and the TZ moves to lower frequencies.

2) When the magnetic coupling dominates ($E_c < M_c$), then $k > 0$ and the TZ appears at the upper stopband. In this case, by increasing the magnetic contribution and keeping the electric one fixed, the total equivalent mixed coupling k increases, as does the BW, and the TZ shifts to a higher frequency. Increasing both equally in magnitude, the TZ moves to lower frequencies without affecting the passband. Increasing the electric contribution and maintaining the magnetic one fixed, k decreases and the TZ moves at lower frequencies.

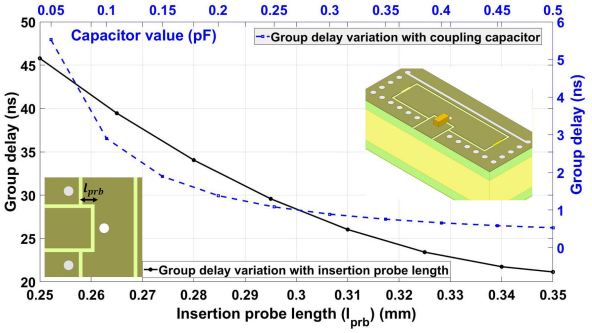

FIGURE 14. Variation of group delay in relation with the insertion probe (black) and SMD coupling capacitors (blue).

It is important to point out that these theoretical models are accurate for narrow bandpass filtering responses. In this paper, a wideband bandpass filter has been designed, then a final optimization process is always necessary to produce the desired response.

B. EXTERNAL COUPLING

The input/output coupling has been implemented by inserting the grounded coplanar line (CPW) into the resonator patch. A larger penetration results in a higher coupling value. The classical approach has been followed for the study of the external quality factor Q_e, employing the reflected group delay $\tau_{S_{11}}$. Thus, the required Q_e can be firstly obtained from the resonator parameters, and the inverter value $J_{0,1}$ [21]

$$Q_e = \frac{Y_0 C_r \omega_0}{J_{0,1}^2} \tag{9}$$

And then, the required extracted group delay can be computed from [25]

$$\tau_{S_{11}} = \frac{4Q_e}{\omega_0} \tag{10}$$

SMD capacitors mounted on the top surface allows the control of the capacitive coupling. As seen from Fig. 14, the assembled SMD capacitors can obtain a very strong coupling, as is usually required for implementing wideband filters. The probe penetration length l_{prb} enables the fine-tuning of the Q_e level for a fixed capacitor value.

C. DESIGN AND OPTIMIZATION PROCESS

The obtained design curves provide an initial point for the filter design. However, fine optimization using full-wave 3D EM simulation of the structure is still required in order to match the target specifications. This approach usually requires extensive simulations, as well as long design and optimization cycles.

However, the proposed structure employing SMD capacitors for resonant frequency and coupling level control, enable us a much more efficient approach for the filter design. Thus, a single and very accurate simulation of the structure including internal ports for the assembled lumped elements is performed. This structure is directly based on the initial values provided by the design curves. Therefore, a multi-port S-parameter matrix is obtained from a full-wave 3D EM simulation.

Then, a very fast optimization approach using circuit level simulations can be performed, by connecting the S-parameter models of the SMD elements to the multi-port matrix of the filter structure (see Fig. 15).

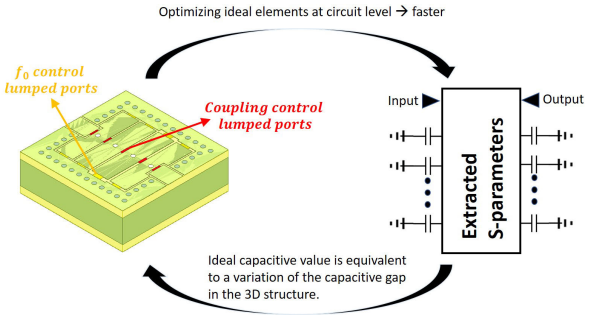

FIGURE 15. Conceptual diagram of the co-simulation process.

Capacitance values connected to the multi-port matrix of the filter can be translated to variations of the capacitive gaps of the structure if required (e.g. for enabling a fine tuning). In this case, a new full-wave simulation is required to update the multi-port matrix. This method allows an accurate and efficient design procedure of the structure with a minimum number of 3D EM simulations. The iterative design procedure is shown in Fig. 16, and is as follows:

1) Generate the coupling matrix based on standard coupling matrix design.
2) Study the frequency behavior of individual resonator, the external couplings, and the couplings between adjacent resonators. Create the coupling variation curves with respect to the physical parameters of the filtering device.
3) Cascade the resonators to obtain the desired order of the filter. As a starting point, implement the physical dimensions to obtain the coupling values obtained in (1).
4) Simulate the 3D structure with lumped ports in order to connect SMD capacitors.
5) Extract the multi-port S-parameter matrix obtained from the full-wave 3D EM simulation, co-simulate the equivalent circuit and optimize the capacitors values to obtain the target filtering response. If the capacitor value (i.e., C_{cap}) is less than the minimum value of real SMD capacitor element (i.e., $C_{cap,min} = 0.05$ pF for AVX Accu-P SMD capacitors used in this work), then adjust the capacitive gap value, otherwise change the SMD element one.
6) Repeat steps (4) and (5) up to match the target in-band response.
7) According to section III, decrease or increase the mixed coupling's magnetic and electrical contributions by the same magnitude to move the zeros in frequency without affecting the BW.

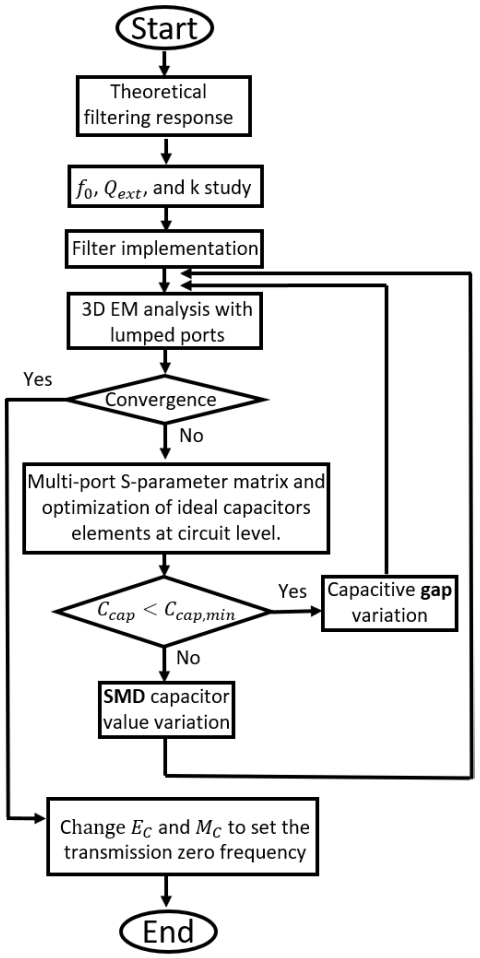

FIGURE 16. Flowchart design process.C_{cap} is the the ideal capacitor element value in the optimized lumped-model equivalent circuit, $C_{cap,min}$ the minimum value of the real SMD elements.

IV. FILTER DESIGN

A 4th-order wideband filter with a Chebyshev response has been designed, manufactured, and experimentally validated to demonstrate the proposed topology, as well as the design and optimization strategies.

The filter is implemented in multi-layer technology to enable a mixed coupling approach, and thus increase the selectivity of the filter by introducing several TZs. The stack-up of the filter has already been introduced previously. Two top and bottom 17 μm copper layers enclose two 0.404 mm-thick RO4350B ($\epsilon_r = 3.55$, $\tan\delta = 0.0037$)

pre-preg (PP) layers, and a dielectric core of 1.524 mm-thick RO4003C ($\epsilon_r = 3.55$, $\tan\delta = 0.0027$). The PP layers are obtained by stacking four 0.101 mm-thick PP laminates. The central resonant frequency of the bandpass filter is set at 5.35 GHz, with a bandwidth of 2.9 GHz (FBW= 54.2%) and a minimum in-band return loss level of 15 dB. Rejection has to be higher than 30 dB at the lower stopband and higher than 20 dB at the upper side. Table 1 summarises the required specifications.

TABLE 1. UWB bandpass filter specifications.

Parameters	U.O.M	Requirements
Central frequency	GHz	5.35
Channel bandwidth	GHz	2.9
Insertion loss at CF	dB	< 5
Over 2900 MHz	dBpp	< 1.5
Over 2500 MHz	dBpp	< 1
7200 MHz to 7800 MHz	dBc	> 20
0 MHz to 3200 MHz	dBc	> 35

As already mentioned, the bandpass center frequency can be controlled by modifying the capacitive value of the resonant cavities. SMD capacitors soldered onto the top layer allow to increase the capacitive value, thus drastically reducing the filter dimensions.

Thus, AVX Accu-P SMD capacitors have been used. Package dimension corresponds to 0201 footprint (i.e. 0.6 × 0.3 mm^2). They are fabricated using thin-film technology to provide a high frequency operational range with low losses up to frequencies above 40 GHz. Capacitor performance for minimum and maximum capacitance values are summarized in Table 2. As can be seen, the self-resonance frequency of 0.6 pF capacitors is around 10 GHz.

TABLE 2. SMD AVX Accu-P 0201 capacitor specifications.

$C(pF)$	$Self resonance(GHz)$	Q	$C_{eff}(pF)$
0.05	20.9	195	0.057
0.6	10.4	135	0.642

The filter has been designed following the previous approach. Firstly, a study of the resonator frequency and coupling values as a function of the main layout parameters has been carried out. The values of the coupling matrix and external quality factor to obtain a 4-order Chebyshev filtering response with FBW= 2.9 GHz, centre frequency $f_0 = 5.35$ GHz, and return loss greater than 15 dB are:

$$|k_{i,j}| = \begin{bmatrix} 0 & 0.4348 & 0 & 0 \\ 0.4348 & 0 & 0.3483 & 0 \\ 0 & 0.3483 & 0 & 0.4384 \\ 0 & 0 & 0.4348 & 0 \end{bmatrix}$$

$$Q_{ext} = 2.21$$

- If $|k_{i,j}| < 0$, TZ appears in the lower stoband.
- If $|k_{i,j}| > 0$, TZ appears in the upper stoband.

After an initial design has been obtained, an optimization process using 3D EM and circuit-level simulations is performed. S-parameters of the SMD capacitors are connected to the multi-port matrix of the filter structure and optimized using a fast circuital simulator. The final filter dimensions meet the electrical specifications, with a final size lower than 7 × 7 mm^2.

A summary of the filter geometrical values is shown in Table 3 and Fig. 17.

TABLE 3. Filter layout parameters and lumped capacitor values.

Resonators capacitive parameters			
Gaps		SMD capacitors	
$g_{p,e1}(mm)$	0.1	$C_{e1} = C_{e1b}(pF)$	0.05
$g_{p,e2}(mm)$	0.1	$C_{e2} = C_{e2b}(pF)$	0.1
$g_{p,e3}(mm)$	0.25	$C_{e3} = C_{e3b}(pF)$	0.1
$g_{p,e4}(mm)$	0.15	$C_{e4} = C_{e4b}(pF)$	0.05
Coupling parameters			
Gaps		SMD capacitors	
$g_{p,co1}(mm)$	0.1	$C_{co1}(pF)$	0.6
$g_{p,co2}(mm)$	0.1	$C_{co2}(pF)$	0.3
$g_{p,co3}(mm)$	0.12	$C_{co3}(pF)$	0.4
$g_{p,co4}(mm)$	0.14	$C_{co4}(pF)$	0.3
$g_{p,co5}(mm)$	0.1	$C_{co4}(pF)$	0.55
Short-circuit stripline probe width			
$dx_{short_{1,2}} = 0.27\ mm$		Layer position: L_2	
$dx_{short_{3,4}} = 0.27\ mm$		Layer position: L_2	
Total filter dimensions			
W(mm)	L(mm)	h(mm)	$d_h(mm)$
7	6,78	2.4	0.25

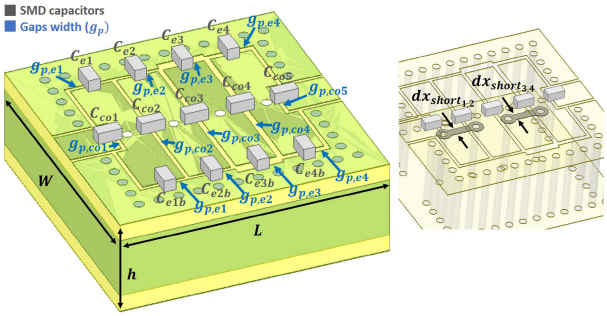

FIGURE 17. Capacitive gaps, SMD capacitors and short-circuit stripline probes in the 3D model.

A. EXPERIMENTAL RESULTS

The SMD capacitors have been assembled on the filter and soldered using a reflow process. The device measurement has been carried out using GSG probes, as shown in Fig. 18.

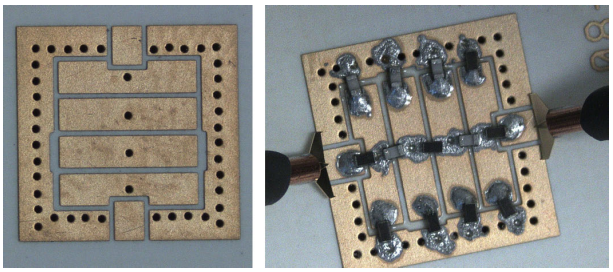

FIGURE 18. Optical microscope photography of the fabricated device (left) and the filter with mounted SMD capacitors (right).

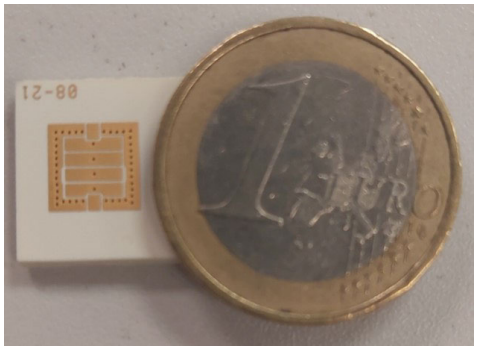

FIGURE 19. Filter prototype before capacitor integration.

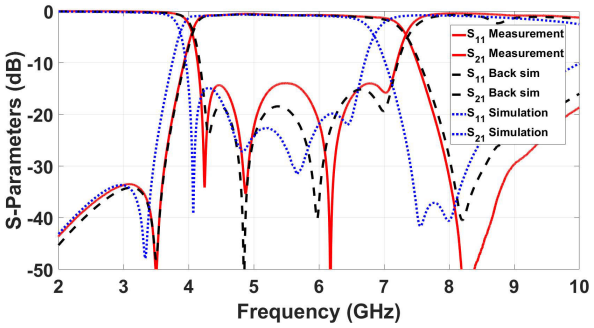

FIGURE 20. Simulated (blue), measured (red) and back-simulated (black) S-parameters of the filter.

As can be seen, the hybrid integration of SMD elements allows for an extremely compact solution. A photo of the manufactured device is shown in Fig. 19.

Experimental results are depicted in Fig.20. Insertion loss at center frequency is 0.75 dB, while in-band return loss is better than 14 dB. As can be seen, a slight frequency shift and higher bandwidth can be observed in the measured response.

B. TOLERANCE ANALYSIS

A manufacturing tolerance analysis has also been carried out. The most critical parameters are the capacitive gaps in the upper layer, the diameter of the inner plated holes, and the thickness of the substrate. Tolerances of $\pm 10\%$ are considered for the capacitive gaps and the via hole diameter, while $\pm 5\%$ is expected for the substrate thickness. These tolerances are representative of standard PCB manufacturing processes. Fig. 21 shows the 3D EM simulated results for variations of the different layout parameters according to the abovementioned tolerances. The width of the copper shorts in the intermediate layers used for magnetic coupling is another parameter that defines the final response of the filter. Larger widths result in higher magnetic coupling value, with a broadening of the pass-band bandwidth, and a shifting of the transmission zeros to a higher frequency.

In coaxial SIW technology, variations of the capacitive gaps can impact the bandwidth and the in-band return loss level. However, in this work, as SMD capacitors present a higher capacitance value, the variation of the surface capacitive gaps due to the manufacturing tolerances does not significantly affect the frequency response of the filtering device (see Fig. 21(b)). In addition, it is possible to adjust the response by modifying the corresponding discrete capacitor values. Therefore, an accurate measurement of the capacitive gaps has been made in the laboratory using an optical microscope. A top view of the measured gap is shown in Fig. 21, where the trapezoidal etching profile is evident. In Fig. 22 and Table 4, the measured and nominal values at the top and bottom (i.e., $W1$ and $W2$, respectively) are summarized. Manufacturing gap tolerances are higher than expected and, combined with the tolerances of the plated holes, dielectric thickness, and inner short-circuit stripline width, produce a response shift in coherence with the measured results. These manufacturing tolerances modify the final response of the filtering device.

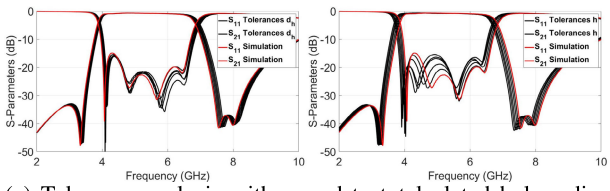

(a) Tolerance analysis with regard to total plated hole radius (d_h) and total thickness (h) tolerances.

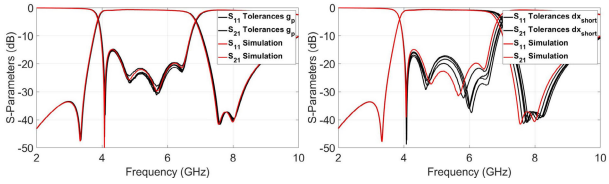

(b) Tolerance analysis with regard to capacitive gap width (g_p) and the inductive copper short width (dx_{short})

FIGURE 21. Ansys HFSS simulated response degradation due to manufacturing tolerances.

C. POST-MANUFACTURING TUNING

A back-simulation has been performed to extract the actual dimensions and capacitor values, with the aim of correcting the center frequency and bandwidth shifts by modifying the corresponding SMD capacitors.

An optimization process is performed to match the measured response by using the circuit-level model of the filter

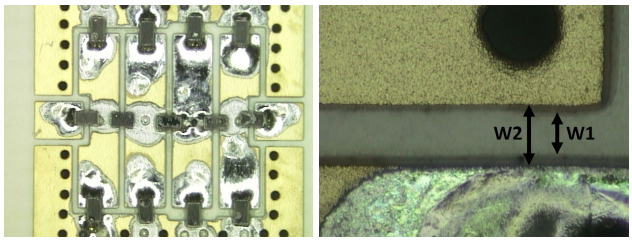

(a) Assembled prototype. (b) Trapezoidal etching profile.

FIGURE 22. Top view captured by an optical microscope.

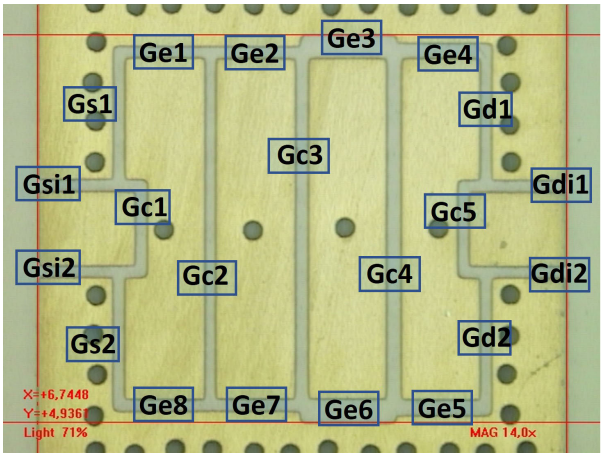

FIGURE 23. Measured gap variables.

(see the back-simulated results in Fig. 20), based on the full-wave 3D EM simulation with internal ports. Then, the modified values can be obtained using the actual capacitance values extracted from the optimization. Lastly, a new filter prototype is assembled with the corrected values.

As can be seen in Table 5, the corrected values taking into account the first exprimental results are close to the nominal ones. Fig. 24 shows the measured results for three different prototypes assembled using the corrected values of the capacitors. As can be seen, a good agreement has been obtained with the targeted response. Return loss level and upper-band rejection are slightly worse than expected, but the center frequency and bandwidth of the filter response have been recovered.

D. COMPARISON WITH OTHER COMPACT SIW DEVICES

As shown in Table 6, the filtering devices proposed in this paper have very compact dimensions compared with other compact SIW technology solutions proposed in the literature. Controllable transmission zeros (TZs) can be implemented thanks to mixed couplings to achieve a more selective filtering response. Despite the significant size reduction, the devices maintain an electrical performance comparable with the other SIW technology solutions. The SMD elements add more flexibility in the filter devices design process, enabling high coupling values control, which is necessary to achieve bandwidths higher than 50%. The post-manufacturing tuning process allows the recovery of the degraded filter response due to manufacturing tolerances.

TABLE 4. Gaps dimension measured with an optical microscope. Variable names are depicted in Fig. 23.

Param	W1(mm)	W2(mm)	WS(mm)
Gsi1	0.1354	0.1822	0.1
Gsi2	0.1262	0.1722	0.1
Gdi1	0.1280	0.1745	0.1
Gdi2	0.1221	0.1696	0.1
Gc1	0.1348	0.1786	0.1
Gc2	0.1149	0.1613	0.1
Gc3	0.1449	0.1898	0.12
Gc4	0.1696	0.2146	0.14
Gc5	0.1248	0.1713	0.1
Gs1	0.1272	0.1751	0.1
Gs2	0.1310	0.1736	0.1
Gd1	0.1292	0.1731	0.1
Gd2	0.1307	0.1742	0.1
Ge1	0.1240	0.1702	0.1005
Ge2	0.1291	0.1787	0.1013
Ge3	0.2754	0.3214	0.25
Ge4	0.1696	0.2162	0.15
Ge5	0.1815	0.2281	0.15
Ge6	0.2868	0.3319	0.25
Ge7	0.1363	0.1839	0.1013
Ge8	0.1325	0.1773	0.1005

TABLE 5. Capacitors back-simulation values. C_S are the first prototype simulated and mounted capacitors values. C_V are the ideal increment values obtained through circuit optimization. C_I and C_R are the values of the ideal and real increments respectively, soldered on the tested prototypes. Fig. 17 shows the SMD capacitors variable names.

Cap	C_S (pF)	C_V (pF)	C_I (pF)	C_R (pF)
C_{co1}	0.6	-0.15	0.75	0.7
C_{co2}	0.3	-0.15	0.45	0.45
C_{co3}	0.4	-0.05	0.45	0.45
C_{co4}	0.3	-0.1	0.4	0.35
C_{co5}	0.55	-0.1	0.65	0.6
C_{e1}	0.05	0	0.05	0.1
C_{e1b}	0.05	0	0.05	0.05
C_{e2}	0.1	-0.05	0.15	0.15
C_{e2b}	0.1	0	0.1	0.1
C_{e3}	0.1	0	0.1	0.15
C_{eb}	0.1	-0.05	0.15	0.1
C_{e4}	0.05	0	0.05	0.05
C_{eb}	0.05	0	0.05	0.05

TABLE 6. Comparison with others compact SIW filtering devices. I.I is the filter reference in section IV.A, I.II the prototype in section IV.C, and II the device in section V.

Ref.	Technology	f_0 (GHZ)	IL (dB)	RL (dB)	Order	BW (%)	Size ($\lambda_g * \lambda_g$)	n_{TZ}	Upper stopband
[9]	dielectric rods SIW	5	1.4	10	4	4	$0.55 * 0.42$	0	20 dB @ $2.20f_0$
[11]	stacked SIW	8.5	1.7	~ 10	3	6.1	$1.1 * 1.05$	3	20 dB @ $2.08f_0$
[26]	multiple-mode SIW	8.5	1.1	11	5	42	$1.25 * 0.63$	1	20 dB @ $1.76f_0$
[27]	dual-mode half-mode SIW	10	2.4	18	4	5.3	$0.89 * 2$	4	30 dB @ $>1.05f_0$
[28]	triple-mode half-mode SIW	11.66	~ 1	11.22	3	29	$0.57 * 1.05$	4	20 dB @$\sim$1.5 f_0
[29]	half-mode SIW	4.5	0.72	20	4	31.1	$0.46 * 0.22$	0	20 dB @ $2.20f_0$
[30]	ridged half-mode SIW	6.43	0.9	20	4	38.3	$0.47 * 0.14$	2	40 dB @ $>1.5f_0$
[31]-I	quarter-mode SIW	3.09	1.28	20	3	15.5	$0.71 * 0.71$	0	20 dB @ $2.01f_0$
[31]-II	eighth-mode SIW	3.09	1.34	15	4	15.2	$0.79 * 0.37$	2	20 dB @ $2.56f_0$
I.I	coaxial SIW	5.66	0.75	14	4	56.1	$0.125 * 0.121$	3	20 dB @ $1.76f_0$
I.II	coaxial SIW	5.35	0.75	13	4	54.2	$0.125 * 0.121$	3	20 dB @ $1.67f_0$
II	coaxial SIW	5.41	0.89	11.7	4	54.9	$0.125 * 0.135$	4	30 dB @ $1.77f_0$

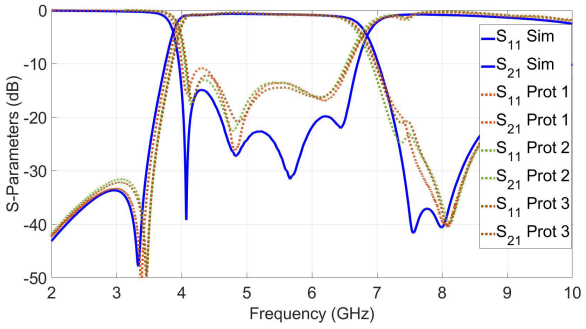

FIGURE 24. Three recovered response prototypes tested compared to simulation response.

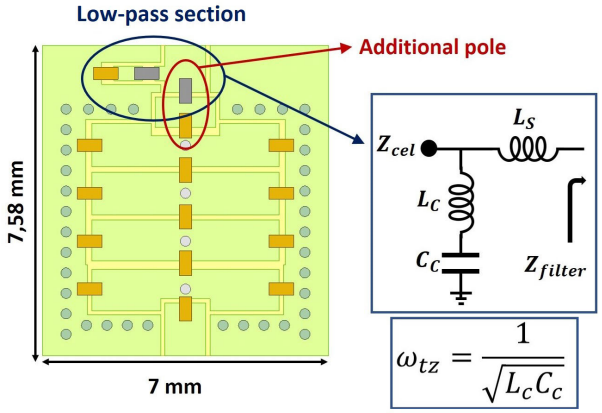

FIGURE 25. 3D Ansys HFSS new structure model (left) and low-pass cell circuit schematic (right). Inductive SMD elements are shown in grey, capacitive ones in orange.

V. ENHANCED OUT-OF-BAND REJECTION

As can be seen in Fig.20, the structure presents low rejection in the upper band probably due to the self resonant frequency of the SMD elements. A new version of the filter with improved performance at higher frequencies has been designed, manufactured and tested. One transmission zero (TZ) has been introduced at the upper band using the approach described in [32], based on a low-pass cell inserted at the input of the bandpass filter (see Fig. 25). The series resonator element C_c and L_c set the position of the upper-band TZ. In order to not affect the filter response, impedance matching conditions are imposed, thus resulting (as detailed in [32]) in:

$$C_c = \frac{\omega_{tz}^2 - \omega_0^2}{\omega_{tz}^2 \omega_0^2} \frac{\sqrt{\frac{Z_{cel}}{Z_{filter}} - 1}}{Z_{cel}} \tag{11}$$

$$L_s = \frac{Z_{filter}\sqrt{\frac{Z_{cel}}{Z_{filter}} - 1}}{\omega_0} \tag{12}$$

The width of the coplanar line at the input of the filter has been increased from 1 mm to 1.47 mm, resulting in an input impedance $Z_{filter} = 45.65\ \Omega$. The input impedance of the low-pass cell has been kept at $Z_{cel} = 50\ \Omega$. After an initial implementation of the SMD elements, the same optimization process as outlined above has been adopted. Ansys HFSS results are depicted in Fig. 26. The series resonator at the input given by the input coupling capacitor and series inductance is responsible for the additional pole in the pass-band response.

A. EXPERIMENTAL RESULTS

To prove the concept, a 4−th order filter has been manufactured and tested. The fabrication parameters are the same as those obtained during the simulations and summarized in

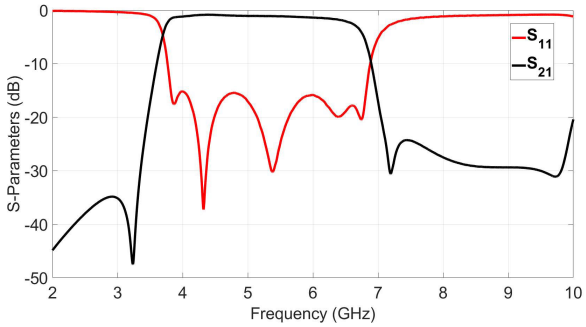

FIGURE 26. EM simulated S-parameters.

TABLE 7. Filter layout parameters and lumped capacitor values, including half section SMD elements value.

Resonators capacitive parameters			
Gaps		SMD capacitors	
$g_{p,e1}(mm)$	0.15	$C_{e1} = C_{e1b}(pF)$	0.1
$g_{p,e2}(mm)$	0.15	$C_{e2} = C_{e2b}(pF)$	0.1
$g_{p,e3}(mm)$	0.15	$C_{e3} = C_{e3b}(pF)$	0.1
$g_{p,e4}(mm)$	0.10	$C_{e4} = C_{e4b}(pF)$	0.1

Coupling parameters			
Gaps		SMD capacitors	
$g_{p,co1}(mm)$	0.1	$C_{co1}(pF)$	0.4
$g_{p,co2}(mm)$	0.13	$C_{co2}(pF)$	0.35
$g_{p,co3}(mm)$	0.12	$C_{co3}(pF)$	0.45
$g_{p,co4}(mm)$	0.2	$C_{co4}(pF)$	0.3
$g_{p,co5}(mm)$	0.1	$C_{co4}(pF)$	0.55

Short-circuit stripline probe width	
$dx_{short_{1,2}} = 0.21\ mm$	Layer position: L_2
$dx_{short_{3,4}} = 0.21\ mm$	Layer position: L_2

Half section elements		
$L_S(nH)$	$C_C(pF)$	$L_C(nH)$
0.68	0.05	0.47

Total filter dimensions			
W(mm)	L(mm)	h(mm)	$d_h(mm)$
7	7.58	2.4	0.25

Tab. 7. The structure is equivalent to the previous filter in Section VI (without the additional high-frequency TZ introduced at the input of the novel structure). The employed dielectric substrate, and stack-up configuration, are the same one used in the previous filter. The new filter prototype is shown in Fig. 27. Due to the same tolerance issues observed with the previous filter, the initial measured response is degraded (see Fig. 28(a)).

As anticipated, an additional pole (due to the series resonator composed of the series connection of the SMD

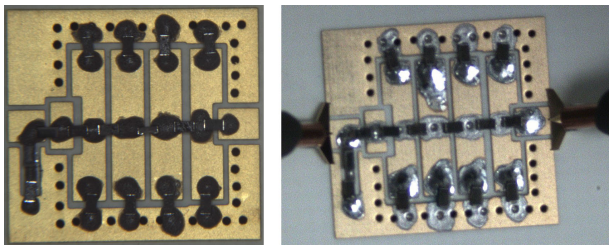

FIGURE 27. Prototype before the soldering process (left) and during testing (right).

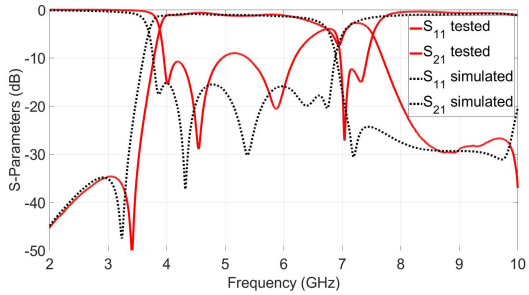

(a) Measured response of the first prototype.

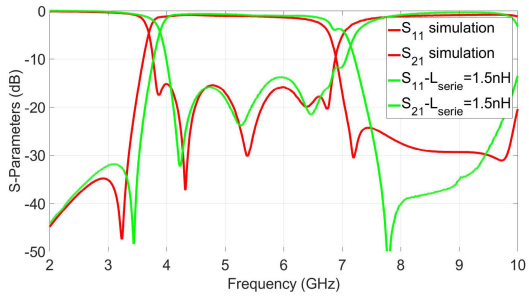

(b) Simulated and $L_S = 1.5$ nH manufactured filter responses.

FIGURE 28. Measured, simulated and post-manufacturing tuned filter response.

inductance and the input coupling capacitance) can be observed. As can be seen in Fig. 28(a), the response is severely degraded where the additional pole is present. A quick back-simulation process shows that by increasing the value of the input inductance, used for impedance matching, the response is improved. As can be seen in Fig. 28(b), with an SMD inductance $L_S = 1.5$ nH the response is enhanced. Insertion loss at center frequency is 0.89 dB, while in-band return loss is better than 11.7 dB. The manufacturing process is the same one used with the previous filter (described in Section IV), so are the related manufacturing tolerances. This is the reason of the observed shift of the filter response.

VI. CONCLUSION

A miniaturized 4th-order wideband bandpass filter based on quasi-lumped SIW technology has been proposed in this paper. To reduce the size and facilitate coupling control, SMD capacitors have been mounted on the top layer. The result is an extremely compact structure. A strong magnetic

coupling between the various resonators has been implemented and superimposed on the capacitive one, resulting in a mixed coupling. Higher total equivalent coupling values can be obtained, allowing for wide bandwidth responses. This mixed coupling has been also employed for introducing transmission zeros, thus improving the filter selectivity. An initial response shift due to manufacturing tolerances has been corrected without further tuning process. In fact, the structure allows the resonator capacitive values and couplings levels reconfigurability thanks to the SMD elements. A second device with improved upper-band rejection has been designed, fabricated, and tested. Again, the response has been recovered thanks to the use of SMD components. The proposed structures can be of great interest for implementing highly integrated filers for emerging flexible payloads.

REFERENCES

[1] D. Deslandes and K. Wu, "Integrated microstrip and rectangular waveguide in planar form," *IEEE Microw. Wireless Compon. Lett.*, vol. 11, no. 2, pp. 68–70, Feb. 2001.

[2] N. Grigoropoulos, B. Sanz-Izquierdo, and P. R. Young, "Substrate integrated folded waveguides (SIFW) and filters," *IEEE Microw. Wireless Compon. Lett.*, vol. 15, no. 12, pp. 829–831, Dec. 2005.

[3] W. Hong, B. Liu, Y. Wang, Q. Lai, H. Tang, X. X. Yin, Y. D. Dong, Y. Zhang, and K. Wu, "Half mode substrate integrated waveguide: A new guided wave structure for microwave and millimeter wave application," in *Proc. Joint 31st Int. Conf. Infr. Millim. Waves 14th Int. Conf. Teraherz Electron.*, Sep. 2006, p. 219.

[4] A. Kumar and A. A. Althuwayb, "SIW resonator-based duplex filtenna," *IEEE Antennas Wireless Propag. Lett.*, vol. 20, no. 12, pp. 2544–2548, Dec. 2021.

[5] D. Chaturvedi, A. Kumar, and S. Raghavan, "Wideband HMSIW-based slotted antenna for wireless fidelity application," *IET Microw., Antennas Propag.*, vol. 13, no. 2, pp. 258–262, Feb. 2019.

[6] Z. Zhang, N. Yang, and K. Wu, "5-GHz bandpass filter demonstration using quarter-mode substrate integrated waveguide cavity for wireless systems," in *Proc. IEEE Radio Wireless Symp.*, Jan. 2009, pp. 95–98.

[7] C. Jin and Z. Shen, "Compact triple-mode filter based on quarter-mode substrate integrated waveguide," *IEEE Trans. Microw. Theory Techn.*, vol. 62, no. 1, pp. 37–45, Jan. 2014.

[8] X. Wang, X.-W. Zhu, Z. Jiang, Z.-C. Hao, Y.-W. Wu, and W. Hong, "Analysis of eighth-mode substrate-integrated waveguide cavity and flexible filter design," *IEEE Trans. Microw. Theory Techn.*, vol. 67, no. 7, pp. 2701–2712, Jul. 2019.

[9] L.-S. Wu, L. Zhou, X.-L. Zhou, and W.-Y. Yin, "Bandpass filter using substrate integrated waveguide cavity loaded with dielectric rod," *IEEE Microw. Wireless Compon. Lett.*, vol. 19, no. 8, pp. 491–493, Aug. 2009.

[10] Y. D. Dong, T. Yang, and T. Itoh, "Substrate integrated waveguide loaded by complementary split-ring resonators and its applications to miniaturized waveguide filters," *IEEE Trans. Microw. Theory Techn.*, vol. 57, no. 9, pp. 2211–2223, Sep. 2009.

[11] W. Shen and H.-R. Zhu, "Vertically stacked trisection SIW filter with controllable transmission zeros," *IEEE Microw. Wireless Compon. Lett.*, vol. 30, no. 3, pp. 237–240, Mar. 2020.

[12] L. Riaz, U. Naeem, and M. F. Shafique, "Miniaturization of SIW cavity filters through stub loading," *IEEE Microw. Wireless Compon. Lett.*, vol. 26, no. 12, pp. 981–983, Dec. 2016.

[13] P. Chu, W. Hong, M. Tuo, K.-L. Zheng, W.-W. Yang, F. Xu, and K. Wu, "Dual-mode substrate integrated waveguide filter with flexible response," *IEEE Trans. Microw. Theory Techn.*, vol. 65, no. 3, pp. 824–830, Mar. 2017.

[14] M. Li, C. Chen, and W. Chen, "Miniaturized dual-band filter using dual-capacitively loaded SIW cavities," *IEEE Microw. Wireless Compon. Lett.*, vol. 27, no. 4, pp. 344–346, Apr. 2017.

[15] J. D. Martínez, S. Sirci, M. Taroncher, and V. E. Boria, "Compact CPW-fed combline filter in substrate integrated waveguide technology," *IEEE Microw. Wireless Compon. Lett.*, vol. 22, no. 1, pp. 7–9, Jan. 2012.

[16] J. D. Martínez, S. Sirci, V. E. Boria, and M. A. Sánchez-Soriano, "When compactness meets flexibility: Basic coaxial SIW filter topology for device miniaturization, design flexibility, advanced filtering responses, and implementation of tunable filters," *IEEE Microw. Mag.*, vol. 21, no. 6, pp. 58–78, Jun. 2020.

[17] E. M. Messaoudi, J. D. Martínez, and V. E. Boria, "Miniaturized ultra-wideband bandpass filter based on substrate integrated quasi-lumped resonators," in *Proc. IEEE MTT-S Int. Microw. Filter Workshop (IMFW)*, Nov. 2021, pp. 201–203.

[18] J. D. Martínez, H. Galindo, S. Sirci, and V. E. Boria, "Miniaturized filters based on SIW quasi-lumped elements," in *Proc. IEEE MTT-S Int. Conf. Numer. Electromagn. Multiphys. Model. Optim. (NEMO)*, Aug. 2018, pp. 1–4.

[19] D. Deslandes and K. Wu, "Accurate modeling, wave mechanisms, and design considerations of a substrate integrated waveguide," *IEEE Trans. Microw. Theory Techn.*, vol. 54, no. 6, pp. 2516–2526, Jun. 2006.

[20] J.-S. Hong and M. J. Lancaster, "Couplings of microstrip square open-loop resonators for cross-coupled planar microwave filters," *IEEE Trans. Microw. Theory Techn.*, vol. 44, no. 11, pp. 2099–2109, Nov. 1996.

[21] J.-S. Hong and M. J. Lancaster, *Microstrip Filters for RF/Microwave Applications*, vol. 167. Hoboken, NJ, USA: Wiley, 2004.

[22] Q.-X. Chu and H. Wang, "A compact open-loop filter with mixed electric and magnetic coupling," *IEEE Trans. Microw. Theory Techn.*, vol. 56, no. 2, pp. 431–439, Feb. 2008.

[23] H. Wang and Q.-X. Chu, "An inline coaxial quasi-elliptic filter with controllable mixed electric and magnetic coupling," *IEEE Trans. Microw. Theory Techn.*, vol. 57, no. 3, pp. 667–673, Mar. 2009.

[24] S. Sirci, J. Martínez, and V. Boria, "A novel magnetic coupling for miniaturized bandpass filters in embedded coaxial SIW," *Appl. Sci.*, vol. 9, no. 3, p. 394, Jan. 2019.

[25] J. B. Ness, "A unified approach to the design, measurement, and tuning of coupled-resonator filters," *IEEE Trans. Microw. Theory Techn.*, vol. 46, no. 4, pp. 343–351, Apr. 1998.

[26] R. S. Chen, S.-W. Wong, L. Zhu, and Q.-X. Chu, "Wideband bandpass filter using U-slotted substrate integrated waveguide (SIW) cavities," *IEEE Microw. Wireless Compon. Lett.*, vol. 25, no. 1, pp. 1–3, Jan. 2015.

[27] F. Zhu, G. Q. Luo, Z. Liao, X. W. Dai, and K. Wu, "Compact dual-mode bandpass filters based on half-mode substrate-integrated waveguide cavities," *IEEE Microw. Wireless Compon. Lett.*, vol. 31, no. 5, pp. 441–444, May 2021.

[28] T. Khorand and M. S. Bayati, "Novel half-mode substrate integrated waveguide bandpass filters using semi-hexagonal resonators," *AEU-Int. J. Electron. Commun.*, vol. 95, pp. 52–58, Oct. 2018.

[29] N. Delmonte, L. Silvestri, M. Bozzi, and L. Perregrini, "Compact half-mode SIW cavity filters designed by exploiting resonant mode control," *Int. J. RF Microw. Comput.-Aided Eng.*, vol. 26, no. 1, pp. 72–79, Jan. 2016.

[30] L. Huang and H. Cha, "Compact ridged half-mode substrate integrated waveguide bandpass filter," *IEEE Microw. Wireless Compon. Lett.*, vol. 25, no. 4, pp. 223–225, Apr. 2015.

[31] P. Li, H. Chu, and R.-S. Chen, "Design of compact bandpass filters using quarter-mode and eighth-mode SIW cavities," *IEEE Trans. Compon., Packag., Manuf. Technol.*, vol. 7, no. 6, pp. 956–963, Jun. 2017.

[32] S. Marín, J. D. Martínez, C. I. Valero, and V. E. Boria, "Microstrip filters with enhanced stopband based on lumped bisected pi-sections with parasitics," *IEEE Microw. Wireless Compon. Lett.*, vol. 27, no. 1, pp. 19–21, Jan. 2017.

EL MEHDI MESSAOUDI (Student Member, IEEE) was born in Fez, Morocco, in 1991. He received the B.S. and M.S. degrees in electronic engineering from the Polytechnic University of Milan, Milan, Italy, in 2016 and 2019, respectively. He is currently pursuing the Ph.D. degree with the Polytechnic University of Valencia. In 2019, he joined the Microwave Application Group (GAM), Institute of Telecommunications and Multimedia Applications (iTEAM), Polytechnic University of Valencia. His current research interests include design and analysis of microwave passive components, with emphasis on new miniaturized solutions for filters based on planar and hybrid technologies, the designing, fabrication, and measurement of tunable microwave substrate integrated waveguide filters using single-layer and multi-layer technologies.

JORGE DANIEL MARTÍNEZ PEREZ (Member, IEEE) was born in Murcia, Spain, in 1979. He received the degree in telecommunication engineering and the Ph.D. degree in electrical engineering from the Universitat Politècnica de València (UPV), Valencia, Spain, in 2002 and 2008, respectively. In 2002, he joined the Department of Electronic Engineering, UPV, as a Research Fellow. In 2007, he was a Visiting Researcher at XLIM CNRS-Université de Limoges, France, working on the design and fabrication of RF MEMS components at the MINACOM Group. He was appointed as an Assistant Professor at UPV, in 2009, and was promoted to an Associate Professor, in 2012. He is currently the Deputy Director of the Department of Electronic Engineering and a Member of the I3M Research Institute at UPV, where he is the Head of the Laboratory for High Frequency Circuits (LCAF), focused on design, manufacturing, and packaging of microwave and mm-wave circuits using planar and multi-layer technologies. He has authored or coauthored more than 80 publications in journals and international conferences. His current research interests include emerging technologies for reconfigurable microwave components, advanced passive devices in planar and substrate integrated waveguide technologies, and multi-layer fabrication technologies for RF/microwave and millimeter-wave applications. He serves as an Associate Editor for IEEE Microwave and Wireless Components Letters and a Regular Reviewer for different journals, including IEEE Transactions on Microwave Theory and Techniques and IEEE Microwave and Wireless Components Letters.

VICENTE E. BORIA (Fellow, IEEE) was born in Valencia, Spain, in May 1970. He received the Ingeniero de Telecomunicación (Hons.) and Doctor Ingeniero de Telecomunicación degrees from the Universidad Politècnica de València, Valencia, in 1993 and 1997, respectively. In 1993, he joined the Departamento de Comunicaciones, Universidad Politécnica de València, where he has been a Full Professor, since 2003. In 1995 and 1996, he was holding a Spanish trainee position with the European Space Research and Technology Centre, European Space Agency (ESTEC-ESA), Noordwijk, The Netherlands, where he was involved in the area of EM analysis and design of passive waveguide devices. He has authored or coauthored ten chapters in technical textbooks, 180 articles in refereed international technical journals, and over 200 papers in international conference proceedings. His current research interests include the analysis and automated design of passive components, left-handed and periodic structures, and on the simulation and measurement of power effects in passive waveguide systems. He has been a member of the IEEE Microwave Theory and Techniques Society (IEEE MTT-S) and the IEEE Antennas and Propagation Society (IEEE AP-S), since 1992. He is also a member of the Technical Committees of the IEEE-MTT International Microwave Symposium and the European Microwave Conference. He is also a member of the European Microwave Association (EuMA). He has been the Chair of the 48th European Microwave Conference held in Madrid, Spain. He acts as a regular reviewer of the most relevant IEEE and IET technical journals on his areas of interest. He was an Associate Editor of the IEEE Microwave and Wireless Components Letters (2013–2018) and *IET Electronics Letters* (2015–2018). He serves as a Subject Editor (*Microwave Journal*) of *IET Electronics Letters* and as an Editorial Board Member of the *International Journal of RF and Microwave Computer-Aided Engineering*.